International Journal of Microwave and Wireless Technologies

cambridge.org/mrf

The impact of the inverse chirp *z*-transform on breast microwave radar image reconstruction

Tyson Reimer[1], Mario Solis-Nepote[2] and Stephen Pistorius[1,2]

[1]Department of Physics and Astronomy, University of Manitoba, Winnipeg, MB, Canada and [2]Research Institute in Oncology and Hematology, University of Manitoba, Winnipeg, MB, Canada

Research Paper

Cite this article: Reimer T, Solis-Nepote M, Pistorius S (2020). The impact of the inverse chirp *z*-transform on breast microwave radar image reconstruction. *International Journal of Microwave and Wireless Technologies* **12**, 848–854. https://doi.org/10.1017/S1759078720000379

Received: 22 November 2019
Revised: 23 March 2020
Accepted: 24 March 2020
First published online: 28 April 2020

Key words:
Microwave imaging; breast imaging; image reconstruction

Author for correspondence:
Tyson Reimer,
E-mail: reimert5@myumanitoba.ca

This work examines the impact of the inverse chirp *z*-transform (ICZT) for frequency-to-time-domain conversion during image reconstruction of a pre-clinical radar-based breast microwave imaging system operating over 1–8 GHz. Two anthropomorphic breast phantoms were scanned with this system, and the delay-multiply-and-sum beamformer was used to reconstruct images of the phantoms, after using either the ICZT or the inverse discrete Fourier transform (IDFT) for frequency-to-time domain conversion. The contrast, localization error, and presence of artifacts in the reconstructions were compared. The use of the IDFT resulted in prominent ring artifacts that were not present when using the ICZT, and the use of the ICZT resulted in higher contrast between the tumor and clutter responses. In one of the phantoms, the tumor response was only visible in reconstructions that used the ICZT. The use of the ICZT evaluated with a time-step size of 11 ps resulted in the reduction of prominent artifacts present when using the IDFT and the successful identification of the tumor response in the reconstructed images.

Introduction

Breast microwave radar imaging has emerged as a potential modality for breast cancer screening [1] due to its use of non-ionizing radiation and relatively low cost. This modality interrogates the breast with an ultrawideband microwave signal, and measurements of the resultant field can be used to reconstruct an image of the breast. Due to the higher dielectric properties of malignant tissues [2], breast microwave imaging (BMI) systems are capable of tumor detection [1, 3].

While radar-based BMI systems perform measurements in the frequency-domain (FD) [4], typically using a vector network analyzer (VNA), or in the time domain (TD) [5], many radar image reconstruction algorithms utilize TD representations of the radar signals, as in the delay-and-sum (DAS) beamformer [6].

BMI systems that perform measurements in the FD require a method for FD-to-TD conversion to utilize TD-based reconstruction algorithms. The inverse discrete Fourier transform (IDFT) and the inverse chirp *z*-transform (ICZT) are two methods that have been used in the literature [4, 7]. Both are special cases of the more general *z*-transform, but the ICZT allows for an arbitrarily-fine representation of the signal in the TD, while the IDFT does not [8].

This work explores the impact of using the ICZT for FD-to-TD conversion in a radar-based BMI system operating over 1–8 GHz. The delay-multiply-and-sum (DMAS) beamformer [9] was used to reconstruct images of two anthropomorphic breast phantoms scanned by a pre-clinical BMI system, and the effects of using the IDFT and the ICZT in the reconstructed images were examined.

Methods

Experimental BMI system and breast phantoms

A pre-clinical radar-based BMI system was used to perform experimental scans of two anthropomorphic breast phantoms. The system uses a VNA (Planar 804/1, Copper Mountain Technologies, Indianapolis, IN, USA) to generate a stepped-frequency continuous-waveform microwave signal at 1001 frequency points over the bandwidth of 1–8 GHz. The system operates in air, without a coupling medium. A complete description of the system can be found in [10]. While the system is capable of bistatic operation, the results presented herein were obtained using a monostatic configuration.

During an experimental scan, the antenna is moved along a circular scan trajectory and the S_{11} scattering parameter is measured at 72 positions along this path. The system measures the scattering parameter in the FD.

Two 3D-printed breast phantoms, representative of the BI-RADS Class I and Class III density classes, were scanned in this investigation [11]. These phantoms were derived from the repository of MRI-based numerical models provided by the University of Wisconsin-Madison [12]. Photographs of the two phantoms used herein are displayed in Fig. 1.

© Cambridge University Press and the European Microwave Association 2020

CAMBRIDGE UNIVERSITY PRESS

A complete description of the phantom manufacturing process is detailed in [11]. Each phantom consists of a fibroglandular shell and an adipose shell. When in use, the fibroglandular shell is inserted into the adipose shell, and both are filled with tissue-mimicking liquids [11]. A 15 mm radius spherical glass bulb filled with saline solution was used as the tumor analog [11].

Signal processing and image reconstruction

The BMI system measures the complex S_{11} scattering parameter in the FD at 1001 points over the range of 1–8 GHz. The DAS beamformer and its derivatives reconstruct an image using TD radar signals. The DMAS beamformer is one such derivative [8], which first performs signal-pair multiplication before synthetically focusing the signals to reconstruct an image,

$$I(\mathbf{r}) = \sum_{m=1}^{M-1} \sum_{n=1+m}^{M} \mathbf{s}_m(t_m(\mathbf{r})) \cdot \mathbf{s}_n(t_n(\mathbf{r})), \tag{1}$$

where $\mathbf{s}_m$ is the mth antenna TD signal, $t_m(\mathbf{r})$ is twice the time-of-flight of the signal from the mth antenna position to the synthetic focal point $\mathbf{r}$, and where the image is displayed as the square of the intensity map $I(\mathbf{r})$. The DMAS beamformer was used to reconstruct images of the two scanned phantoms.

The BMI system measures in the FD, and the signals must be converted to the TD for reconstruction via the DMAS beamformer. For FD-to-TD conversion, either the IDFT or ICZT can be used. The IDFT is defined as

$$\mathbf{s}(n) = \frac{1}{N} \sum_{k=0}^{N-1} \mathbf{S}(k) \exp\left(\frac{j2\pi kn}{N}\right), \tag{2}$$

where $\mathbf{s}(n)$ is the discrete TD radar signal, $\mathbf{S}(k)$ is the discrete FD measured signal of length N, and $n = 0, 1, \ldots, N-1$ [8]. This conversion results in a TD signal with step-size $\Delta t = 1/F_{span}$, where F_{span} is the frequency span of the FD signal [8]. For the experimental system used in this study (operating over 1–8 GHz), this results in a TD radar signal with step-size $\Delta t \approx 0.143$ ns. In air, this corresponds to a distance step-size of approximately 43 mm.

The IDFT is a special case of the z-transform, evaluated at particular values of z, evenly spaced along the unit circle in the z-plane. The ICZT is also a special case of the z-transform and can be generally evaluated at any point in the complex z plane, but for the purposes of FD-to-TD conversion will only be examined along the unit circle. In this special case, the ICZT is defined (within a scaling factor) as

$$\mathbf{s}(n) = \frac{1}{N} \sum_{k=0}^{N-1} \mathbf{S}(k) \exp\left(j\theta_0 k\right) \exp\left(j\phi_0 kn\right), \tag{3}$$

where the parameters θ_0 and ϕ_0 allow for the selection of the time-span of the signal $\mathbf{s}(n)$ and $n = 0, 1, \ldots, L-1$, where L can be selected as an arbitrary integer. The ICZT produces a TD signal $\mathbf{s}(n)$, represented by L points along the arc starting at angle $\omega_i = \theta_0$ and ending at the angle $\omega_f = (L-1)\phi_0 + \theta_0$. These angles ω_i and ω_f can be converted to true time values t_i, t_f that describe the start and end points of the TD signal $\mathbf{s}(n)$ [8].

The ICZT allows for an arbitrarily-fine representation (because of the parameter L) of the FD signal $\mathbf{S}(k)$ in the TD over a specified time-span (because of the parameters θ_0 and ϕ_0). Figure 2 displays sample measured signals from an experimental phantom scan when the FD-to-TD conversion is performed using the IDFT and the ICZT.

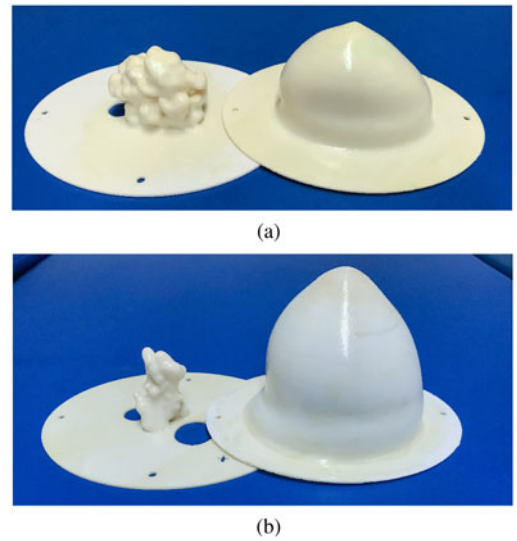

Fig. 1. 3D-printed MRI-based breast phantoms used in this investigation. Fibroglandular (left) and adipose (right) shells used to create a Class III phantom in (a), and a Class I phantom in (b).

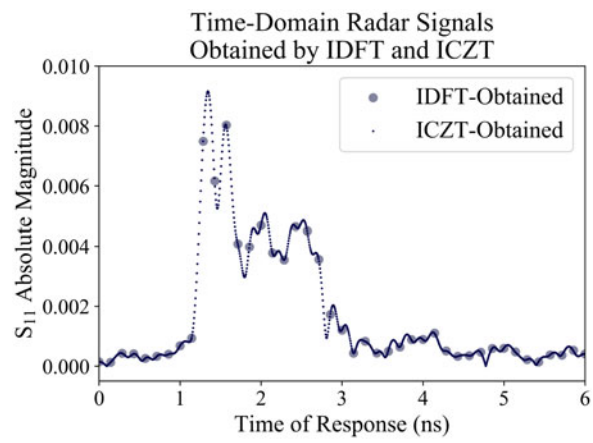

Fig. 2. TD radar signals obtained using the IDFT and ICZT (evaluated at 1024 points between 0 and 6 ns response times). Signals obtained from one antenna position from an experimental scan of the Class III breast phantom.

In a stepped-frequency continuous-waveform system, a discrete measurement is made in the FD. In a TD radar system [5], a continuous signal is sampled and stored as a discrete TD signal. Just as the sampling frequency in a TD system determines the time-step size, the choice of the parameter L determines the step-size of the TD representation of the signal obtained using a FD system. As the sampling frequency becomes large, TD measurements approach the continuous representation of the signal, and as $L \to \infty$, so too does the $\mathbf{s}(n)$ signal obtained by the ICZT.

Image quality metrics

While a comparison between the impact of the IDFT and ICZT in the sinogram-space is ideal (as such a comparison would be independent of the choice of image reconstruction algorithm), the

https://doi.org/10.1017/S1759078720000379 Published online by Cambridge University Press

sinograms created via either the IDFT or ICZT have dimensionalities determined by the number of time-steps. Although comparisons in the image-space are dependent on the choice of reconstruction method, image-based comparisons overcome the different dimensionalities in the sinogram-space. For this reason, this work presents an analysis using the reconstructed images produced using a widely used DAS-based beamformer.

Two image quality metrics were used to quantitatively compare the contrast in the reconstructions produced by the DMAS beamformer after using the ICZT or the IDFT for FD-to-TD conversion. The signal-to-mean ratio (SMR) was defined as

$$\mathrm{SMR} = 20\log_{10}\left(\frac{S_{max}}{C_{mean}}\right), \tag{4}$$

where S_{max} is the maximum response in the known tumor region, and C_{mean} is the mean response in the clutter region (defined to be the region of the image belonging to the phantom but not to the tumor). The signal-to-clutter ratio (SCR) was defined as

$$\mathrm{SCR} = 20\log_{10}\left(\frac{S_{max}}{C_{max}}\right), \tag{5}$$

where C_{max} is the maximum response in the clutter region. The uncertainty in C_{mean} was assumed to be zero, the uncertainty in S_{max} was defined to be the standard deviation of the intensity of the 75th percentile of pixels in the tumor region, and the uncertainty in C_{max} was defined to be the standard deviation of the intensity of the 95th percentile of pixels in the clutter region. The SMR and SCR provide a measure of the contrast between the tumor response and the clutter response in the reconstructed images.

To evaluate the accuracy of the tumor response in the images, the localization error l of the tumor response was determined for each reconstruction, defined as

$$l = |\mathbf{r}_{meas} - \mathbf{r}_{img}|, \tag{6}$$

where $\mathbf{r}_{meas}$ is the measured location of the tumor and $\mathbf{r}_{img}$ is the location of the maximum response within the image.

Results

The DMAS reconstructions of the BI-RADS Class I phantom are displayed in Fig. 3(a) when using the IDFT for FD-to-TD conversion and in Fig. 3(b) when using the ICZT evaluated using 1024 time points.

The tumor response is prominent in both reconstructions. However, ring artifacts are present in the images obtained after using the IDFT for FD-to-TD conversion. These ring artifacts are absent in the ICZT-obtained images. While these artifacts do not completely obfuscate the presence of the tumor response in the case of the Class I phantom in Fig. 3(a), they do distort the tumor response when compared to the ICZT-obtained image in Fig. 3(b).

The reconstructions of the Class III phantom are displayed in Fig. 4. The tumor response in the IDFT-obtained image in Fig. 4(a) is completely obfuscated by the clutter responses outside of the known tumor position. For this phantom scan, only the ICZT-obtained reconstruction displays the tumor response. The prominent ring artifacts observed in the IDFT-obtained reconstruction of the Class I phantom are also present in Fig. 4(a).

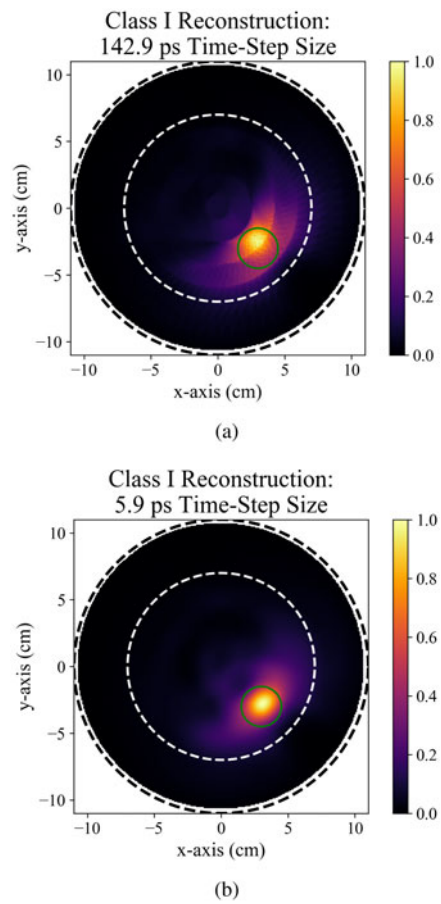

Fig. 3. DMAS reconstructions of a 15 mm radius lesion in a Class I phantom using (a) the IDFT and (b) the ICZT. The solid green circle indicates the tumor location, the dotted white circle indicates the approximate phantom boundary, and the dotted black circle indicates the antenna trajectory during the scan. Each image is normalized to its maximum intensity value.

The SMR of each image is displayed in Fig. 5, while the SCR is displayed in Fig. 6. While no significant difference in either contrast metric was observed for the Class I images (obtained after using either the IDFT or the ICZT for FD-to-TD conversion), the SMR of the ICZT-obtained Class III image was significantly greater than that of the IDFT-obtained image. The negative SCR of the IDFT-obtained image of the Class III image indicates that the tumor response was not identifiable in the reconstruction because the largest response in the image occurred outside of the known tumor region. This can be observed directly in Fig. 4(a).

While the use of the IDFT did not significantly affect either contrast metric in the low-density Class I phantom, the negative SCR in the IDFT-obtained Class III reconstruction demonstrates that the use of the IDFT can be detrimental to image-based tumor identification in a BMI system.

Discussion

Optimization of ICZT parameters

The results in Fig. 4 indicate that tumor detection is dependent on the choice of the time-step size used to represent the TD radar signals. To examine the minimum time-step size required for tumor detection in the case of this Class III phantom, the localization error for reconstructions produced using several time-step

https://doi.org/10.1017/S1759078720000379 Published online by Cambridge University Press

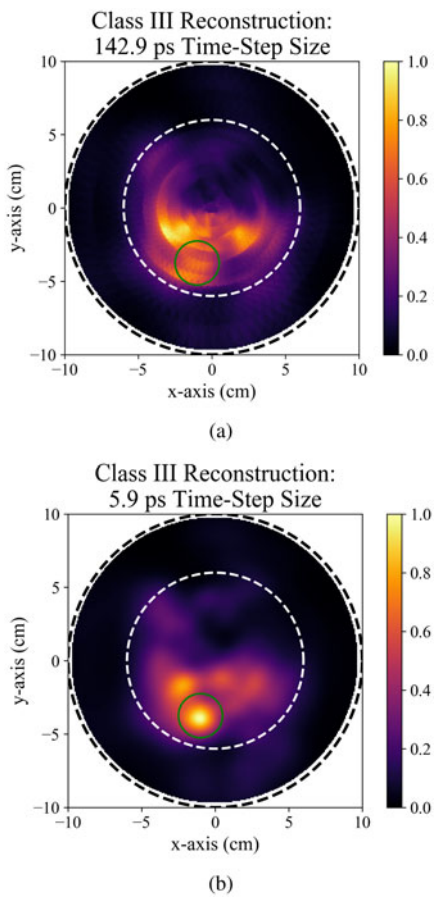

Fig. 4. DMAS reconstructions of a 15 mm radius lesion in a Class III phantom using (a) the IDFT and (b) the ICZT. The solid green circle indicates the tumor location, the dotted white circle indicates the approximate phantom boundary, and the dotted black circle indicates the antenna trajectory during the scan. Each image is normalized to its maximum intensity value.

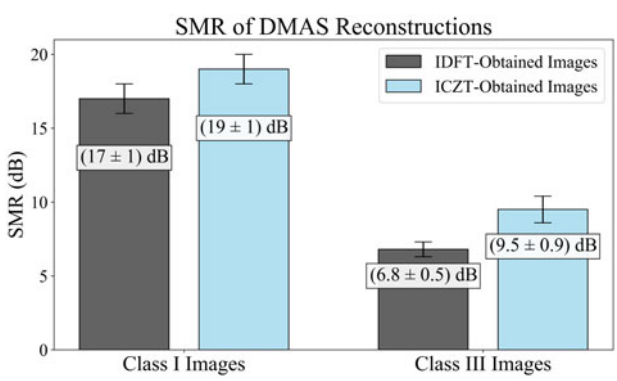

Fig. 5. SMR of the DMAS reconstructions produced after using either the IDFT or the ICZT (evaluated at 1024 time-points between 0 and 6 ns response times).

sizes were determined and are displayed in Fig. 7. The localization error can be used as a tumor detection criterion, where the tumor is defined to be detected if the localization error was less than the radius of the tumor, indicating the maximum response in the image did occur within the known tumor region.

The results in Fig. 7 indicate that for time-step sizes less than 4 ps, the localization error in the image is unchanged, and for time-

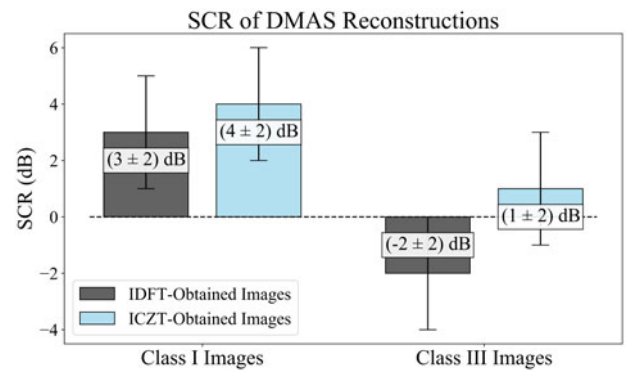

Fig. 6. SCR of the DMAS reconstructions produced after using either the IDFT or the ICZT (evaluated at 1024 time-points between 0 and 6 ns response times).

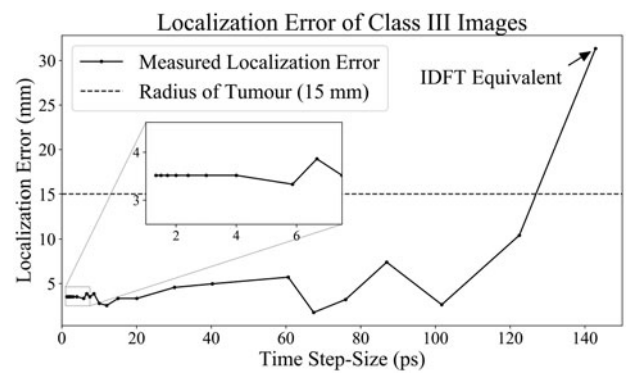

Fig. 7. Localization error of the Class III reconstructions as a function of the time-step size. The dotted line indicates the radius of the tumor.

step sizes smaller than 20.1 ps (corresponding to 300 time-points used in the ICZT over 0–6 ns), the change in localization error is less than 1 mm. For time-step sizes smaller than 142.9 ps, the localization error is smaller than the radius of the tumor, indicating the largest response in the image occurred within the known tumor region. Given this, from Fig. 7, all time-step sizes $\Delta t <$ 142.9 ps allow for an identifiable tumor response in the reconstructed image. These results set an upper-bound on the size of the time-step required for tumor detection. However, these results do not contain any information regarding the ring artifacts observed in the reconstructions.

The use of the ICZT, evaluated using a time-step size of 5.9 ps, is sufficient for tumor-detection for the Class III phantom and does not contain ring artifacts, as displayed in Fig. 4. To evaluate the impact of time-step size on the reconstructed image, Fig. 8 displays images of the Class III phantom for four choices of time-step size, varying from 142.9 ps (equivalent to the IDFT) to 10.9 ps. The reconstructions in Figs. 8(a)–8(c) contain prominent ring artifacts, but these artifacts are indiscernible in Fig. 8(d), as they are in Fig. 4(b).

These ring artifacts are present in reconstructions of both the Class III phantom (as in Fig 4) and the Class I phantom (as in Fig 3). To quantify the relative prominence of these artifacts, the total absolute-difference between images produced using various time-step sizes (greater than 5.9 ps) and the image produced using 5.9 ps time-step size were determined.

https://doi.org/10.1017/S1759078720000379 Published online by Cambridge University Press

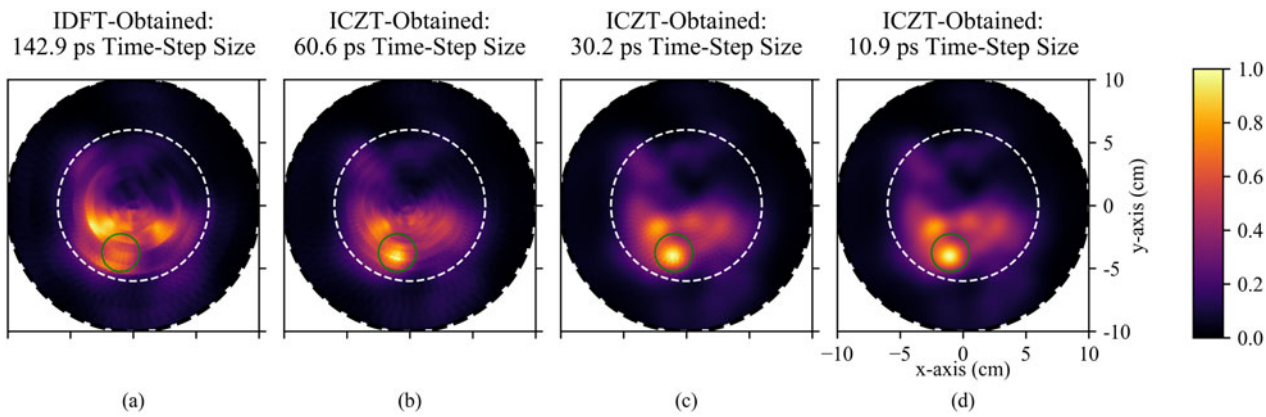

Fig. 8. DMAS reconstructions of a 15 mm radius lesion in a Class III phantom using (a) the IDFT, (b) the ICZT with 100 time-points from 0 to 6 ns (60.6 ps time-step size), (c) the ICZT with 200 time-points (30.2 ps time-step size), and (d) the ICZT with 550 time-points (10.9 ps time-step size).

This total absolute-difference D is defined as

$$D = \sum_{i,j} |\sigma_{i,j}^{tar} - \sigma_{i,j}^{ref}|, \tag{7}$$

where $\sigma_{i,j}^{tar}$ is the intensity of the pixel at index (i, j) in the target image and $\sigma_{i,j}^{ref}$ is the intensity of the pixel at index (i, j) in the reference image (the image reconstructed after evaluating the ICZT at 1024 time-points over 0–6 ns).

While this metric does not specifically quantify the ring artifacts in the images, it is clear from Fig. 8 that the most prominent differences in the DMAS reconstructions of the Class III phantom, produced using different time-step sizes, are due to the presence of ring artifacts. Given that the image produced using a time-step size of 5.9 ps has the least prominent artifacts, the total absolute difference provides a measure of the relative impact of the ring artifacts on the image.

If the difference metric D is determined by the width of the ring artifacts, then D should exhibit a linear relationship with respect to the time-step size used in the ICZT (equivalently, an inverse relationship to the number of time-points used). The ring widths w_{ring} are hypothesized to be proportional to the time-step size used in the ICZT,

$$w_{ring} = v_{avg}\Delta t, \tag{8}$$

where v_{avg} is the estimated average propagation speed used in the reconstruction method. Because DAS-based beamformers back-project the radar signals onto the image-space using the time-of-flight to determine the localization of a radar response, the spatial arcs (assuming uniform propagation speed) that correspond to a particular time-of-response t of a measured radar response from one antenna position correspond to the positions $\mathbf{r}$ such that

$$v_{avg}\left(t - \frac{\Delta t}{2}\right) \leq |\mathbf{r}| \leq v_{avg}\left(t + \frac{\Delta t}{2}\right). \tag{9}$$

The width of these arcs is therefore determined by the parameter Δt, and $\Delta t \propto 1/N$ where N is the number of time-points used in the ICZT over a specified time-window. If the ring artifacts in the images are caused by Δt, as is hypothesized, and if the total absolute difference metric D is primarily determined by the differences in the ring-artifacts between images, then D will also be inversely proportional to N.

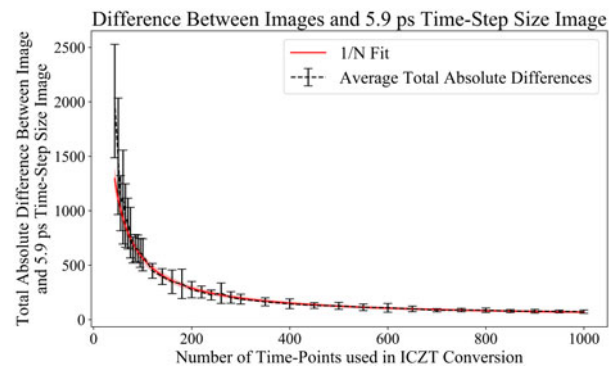

Fig. 9. Average total absolute-difference of images produced using time-step sizes greater than 5.9 ps and the image produced after using the ICZT for FD-to-TD conversion with a time-step size of 5.9 ps, for 10 scans of the Class III phantom. Standard deviations of the average total absolute-difference over the images from the 10 scans are the displayed uncertainties. The shaded red region indicates the 99.7% confidence intervals on the fit.

To determine the variation of this difference metric D across scans of the same phantom, ten scans of the Class III phantom were performed. The average values of the metric D across the reconstructions of the ten scans are displayed in Fig. 9. The hypothesized inverse relationship between D and N was evaluated by fitting the relationship

$$D = \frac{a}{N} + b \tag{10}$$

to the measured values, where a and b were the fit parameters. The fit is displayed in red in Fig. 9, with the 99.7% confidence intervals displayed in the transparent shaded red region.

The results in Fig. 7 indicate an asymptotic relationship between the number of time-points used (inversely proportional to the time-step size) and the total absolute difference between the reconstructed image and the reference image (produced using the 1024 time-point ICZT). The hypothesized relationship agrees with all but the first measured point in the figure,

https://doi.org/10.1017/S1759078720000379 Published online by Cambridge University Press

indicating the width of the ring artifacts is caused by the time-step size used in the ICZT.

These results indicate that the circular artifacts are caused by the time-step size used to represent the TD radar signals, and because the ICZT allows for manual selection of time-step size, the choice of an appropriately small time-step eliminates these artifacts (as in Fig 8(d)).

The image reconstructed using 550 time-points (equivalent to a time-step size of 10.9 ps) was the image produced with the largest time-step that produced a difference metric D that agreed with the difference metric of reconstruction produced using 1000 time-points, within the reported uncertainties. This result indicates that the artifacts are not significantly different between these reconstructions. This can be seen by comparing Figs. 4(b) and 8(d). A time-step size of $\Delta t < 10.9$ ps is therefore sufficient for artifact reduction.

The results in Fig. 7 indicate that reducing the time-step size from that obtained via the IDFT is sufficient for tumor detection, and the results in Fig. 9 indicate the prominence of the ring artifacts is reduced after using $N \geq 550$ time-points (corresponding to 10.9 ps). For the BMI system used in this work, operating over 1–8 GHz, the use of a 10.9 ps time-step size is sufficient for both tumor-detection and artifact-reduction in the reconstructed images presented herein.

Relation to other BMI systems

The ICZT has been used in other radar-based BMI systems [7] and was also found to have increased the SCR in reconstructed images (using the DAS beamformer, as described in [13]). The system used in [7] operated over the frequency range of 50 MHz to 20 GHz, resulting in a time step of $\Delta t \approx 50$ ps. The clinical BMI system used in this work operates over the narrower bandwidth of 1–8 GHz, resulting in a larger time-step of $\Delta t \approx$ 142.9 ps. The larger time-step size of the system presented herein causes the ring artifacts to be more prominent in the reconstructions (due to the larger width of the artifacts). The ring artifacts produced using the IDFT in the larger bandwidth system in [7] are expected to be $\approx \frac{1}{3}$ as wide as those obtained with our system. Those artifacts are less prominent than those obtained with our system in Fig. 8(a) but are similar to the reconstruction in Fig. 8(c), where the prominence of the ring artifacts has been reduced.

While this investigation examined the effects of the ICZT on image reconstruction when using the DMAS beamformer, the results obtained in this work may apply when using other DAS-based methods that synthetically focus the measured radar signals. Previous work in [14] proposed the use of an iterative reconstruction algorithm for breast microwave radar and used the IDFT for FD-to-TD conversion. The impact of using the ICZT with the algorithm proposed in [14] is expected to have a similar effect to that observed in this work when using the DMAS method, as both are derivatives of the DAS beamformer and rely on synthetically focusing the measured radar signals.

Conclusion

This work examined the impact of using the IDFT and ICZT for FD-to-TD conversion in a radar-based BMI system on image reconstruction. Two anthropomorphic phantoms were scanned with a clinical radar-based BMI system operating over 1–8 GHz, and the DMAS beamformer was used to reconstruct images of the phantoms. The use of the IDFT resulted in lower SMR and SCR than when using the ICZT in reconstructions of both phantoms and resulted in the presence of prominent ring artifacts in both images. In the reconstructions of the Class III phantom, the image produced using the IDFT did not display the tumor response, while the use of the ICZT allowed for more accurate synthetic focusing of the radar signals, resulting in a prominent tumor response. Reconstructions produced after using the ICZT with a time-step size of 10 ps had less prominent artifacts than those produced with the IDFT, and resulted in an identifiable tumor response.

Acknowledgements. The authors would like to thank the National Science and Engineering Research Council of Canada, the University of Manitoba, and the CancerCare Manitoba Foundation for helping to fund this work.

References

1. **Nikolova N** (2011) Microwave imaging for breast cancer. *IEEE Microwave Magazine*, **12**, 78–94.
2. **Sugitani T, Kubota S, Kuroki S, Sogo K, Arihiro K, Okada M, Kadoya T, Hide M, Oda M and Kikkawa T** (2014) Complex permittivities of breast tumor tissues obtained from cancer surgeries. *Applied Physics Letters*, **104**, article number 253702.
3. **Grzegorczyk T, Meaney P, Kaufman P, diFlorio-Alexander R and Paulsen K** (2012) Fast 3-D tomographic microwave imaging for breast cancer detection. *IEEE Transactions on Medical Imaging*, **31**, 1584–1592.
4. **Flores-Tapia D, Rodriguez D, Solis M, Kopotun N, Latif S, Maizlish O, Fu L, Gui Y, Hu C-M and Pistorius S** (2016) Experimental feasibility of multistatic holography for breast microwave radar image reconstruction. *Medical Physics*, **43**, 4674–4686.
5. **Porter E, Kirshin E, Santorelli A, Coates M and Popović M** (2013) Time-domain multistatic radar system for microwave breast screening. *IEEE Antennas and Wireless Propagation Letters*, **12**, 229–232.
6. **Hagness S, Taflove A and Bridges J** (1998) Two-dimensional FDTD analysis of a pulsed microwave confocal system for breast cancer detection: fixed-focus and antenna-array sensors. *IEEE Transactions on Biomedical Engineering*, **45**, 1470–1479.
7. **Fear E, Sill J and Stuchly M** (2003) Experimental feasibility study of confocal microwave imaging for breast tumor detection. *IEEE Transactions on Microwave Theory and Techniques*, **51**, 887–892.
8. **Frickey D** (1994) Using the inverse chirp-z transform for time-domain analysis of simulated radar signals, *Proceedings of the 5th International Signal Processing Applications and Technology Conference*, *United States Department of Energy*, Dallas, Texas, United States, pp. 1366–1371.
9. **Lim HB, Nhung NTT, Li E-P and Thang ND** (2008) Confocal microwave imaging for breast cancer detection: delay-multiply-and-sum image reconstruction algorithm. *IEEE Transactions on Biomedical Engineering*, **55**, 1697–1704.
10. **Solis-Nepote M and Reimer T and Pistorius S** (2019) An air-operated bistatic system for breast microwave radar imaging: pre-clinical validation. *Engineering in Medicine and Biology Conference 2019, IEEE*, Berlin, Germany.
11. **Rodriguez-Herrera D, Reimer T, Solis-Nepote M and Pistorius S** (2017) Manufacture and testing of anthropomorphic 3D-printed breast phantoms using a microwave radar algorithm optimized for propagation speed. *2017 11th European Conference on Antennas and Propagation (EUCAP)*, IEEE, Paris, France, pp. 3480–3484.
12. **Burfeindt M, Colgan T, Mays RO, Shea J, Behdad N, Veen BV and Hagness S** (2012) MRI-derived 3-D-printed breast phantom for microwave breast imaging validation. *IEEE Antennas and Wireless Propagation Letters*, **11**, 1610–1613.
13. **Fear E, Li X, Hagness S and Stuchly M** (2002) Confocal microwave imaging for breast cancer detection: localization of tumors in three dimensions. *IEEE Transactions on Biomedical Engineering*, **49**, 812–822.
14. **Reimer T, Rodriguez-Herrera D, Solis-Nepote M and Pistorius S** (2018) The use of a novel microwave radar reconstruction algorithm to image

https://doi.org/10.1017/S1759078720000379 Published online by Cambridge University Press

lesions in realistic 3D breast phantoms. *2018 12th European Conference on Antennas and Propagation (EuCAP)*, *IET,* London, UK.

Tyson Reimer received his B.Sc. in medical & biological physics from the University of Manitoba in 2018 and is pursuing an M.Sc. degree in medical physics at the University of Manitoba.

Mario Solis-Nepote obtained his B.Sc. degree in mechatronics engineering from Tecnológico de Monterrey, Campus Chihuahua, Mexico, in 2010, and his M.Sc. in biomedical engineering from the University of Manitoba, in 2018, for his work in the development of clinical tools for microwave breast cancer detection. From 2017 to 2019, he was the main graduate research associate at the Non-Ionizing Imaging Laboratory at the University of Manitoba. He is currently working with advanced metrology and quality control projects at Boeing Canada. His research interests are focused on the design and development of medical devices and in the applications of machine learning for the medical and aerospace industries.

Stephen Pistorius is a tenured Professor and Associate Head: Medical Physics in Physics and Astronomy and Professor in Radiology at the University of Manitoba. He serves as the Vice Director and Graduate Chair of the Biomedical Engineering Program and is a Senior Scientist at the Research Institute in Oncology and Hematology. He holds a Hons. B.Sc. (radiation physics), M.Sc. (medical science), and Ph.D. (physics) from the University of Stellenbosch, South Africa, and a Post-Graduate Diploma in Business Management from the Edinburgh Business School, UK. His research interests focus on image processing and reconstruction, medical device development, improving, optimizing, and quantifying various diagnostic and therapeutic techniques and in modeling and understanding radiation transport in clinically useful imaging and treatment modalities.

https://doi.org/10.1017/S1759078720000379 Published online by Cambridge University Press